



TrackDip: a multi-scale processing of dipmeter data. Method, tests, and field example for 3D description of gravity-driven deformations in the Eocene foreland basin of Ainsa, Spain

Christophe Basile, Arnaud Pécher, Matthieu Corazzi, Francis Odonne, Agnès Maillard, Elie Jean Debroas, Pierre Callot

► To cite this version:

Christophe Basile, Arnaud Pécher, Matthieu Corazzi, Francis Odonne, Agnès Maillard, et al.. TrackDip: a multi-scale processing of dipmeter data. Method, tests, and field example for 3D description of gravity-driven deformations in the Eocene foreland basin of Ainsa, Spain. 2007. hal-00124633v1

HAL Id: hal-00124633

<https://hal.science/hal-00124633v1>

Preprint submitted on 15 Jan 2007 (v1), last revised 12 Mar 2008 (v2)

HAL is a multi-disciplinary open access archive for the deposit and dissemination of scientific research documents, whether they are published or not. The documents may come from teaching and research institutions in France or abroad, or from public or private research centers.

L'archive ouverte pluridisciplinaire **HAL**, est destinée au dépôt et à la diffusion de documents scientifiques de niveau recherche, publiés ou non, émanant des établissements d'enseignement et de recherche français ou étrangers, des laboratoires publics ou privés.

Multi-scale processing of dipmeter data: field example for 3D description of gravity-driven deformations in the Eocene foreland basin of Ainsa, Spain

C. Basile^{1*}, A. Pecher¹, M. Corazzi¹, F. Odonne², A. Maillard², E.J. Debrosas², P. Callot²

1 : Laboratoire de Géodynamique des Chaînes Alpines, CNRS-UMR 5025, Observatoire des Sciences de l'Univers de Grenoble, Université Joseph Fourier, BP 48, 38041 Grenoble Cedex, France. Fax 334 7651 4058

2 : Laboratoire de Mécanismes de Transfert en Géologie, CNRS-UMR 5563, Observatoire Midi Pyrénées, Université Paul Sabatier, 14 Avenue Edouard Belin, 31400 Toulouse, France. Fax 335 6133 2560.

* Corresponding author : cbasile@ujf-grenoble.fr

Abstract

This paper presents a new method for dipmeter data processing, that identify significant tilts based on a multi-scale approach. We tested this method on a field example, along three sections in the Eocene Sobrarbe delta, Ainsa foreland basin, northern Spain. The sedimentary and tectonic structures, especially the three main syn-sedimentary sliding surfaces (S1 to S3) observed on the field, were successfully identified from processed dipmeter data.

The tilt axis are mainly trending N-S in sandstones, associated to westward transport of sediments. The sliding surfaces S1 and S3 correspond to E-W-trending tilt axis, tentatively correlated either to the flexural subsidence of the basin, or to anticline growth during sedimentation south of the studied area. Combination of these sedimentary and tectonic directions results in a NE-SW trending submarine slope, that locally controls the gravity-driven deformations, especially on S2 the sliding surfaces. Finally, NNW-SSE-trending tilts above the uppermost S3 sliding surface are interpreted as the result of infilling on the side of the scar produced by sliding.

Keywords : dipmeter, tilt, processing, gravity-driven deformations, foreland basin

Introduction

Among downhole logging tools, dipmeters represent a class of tools designed to measure the orientation, i.e. both dip and dip direction (azimuth), of the planes intersected by a borehole. While borehole are one-dimensional, dipmeter data allow to describe 3-D geometry of sedimentary units, and bring crucial informations on all processes involving changes of orientation in sediment bedding, such as deposition in flows (e.g. Luthi and Banavar, 1988 ; Höcker et al., 1990 ; Donselaar and Schmidt, 2005), deformations during and after sedimentation (e.g. Hesthammer and Fossen, 1998), differential subsidence. It is noteworthy that these changes of orientation occur at various space and time scales, and that their effects are merged in a single record.

However, the word dipmeter refers only to dip measurements, and little has been done to fully use these three-dimensional measurements. The classical tadpole graphical display of dip and azimuth as a function of depth (Serra, 1989) underlines the dip variations, but azimuth variations are uneasy to read. Interpretations often used mainly dip variations (Gilreath, 1987 ; Serra, 1989). Similarly, processing methods either used only dip measurements (Hurley, 1994), or are restricted to a given scale (point to point analysis : Berg, 1998 ; folded structures : Bengtson, 1981).

In this article, we present a new method to process bedding attitudes in order to identify at various scales the successive changes of orientations in a sedimentary section. While designed to process dipmeter logging data, we tested this method on a field example, in the Eocene foreland basin of Ainsa (Spain). This test allows a direct comparison between interpretations from dipmeter analysis and outcrop exposures.

Processing dipmeter data

The processing methodology described herein is a formalized version of the empirical process used by Basile (2000) on logging data. Annexes 1 to 4 present the successive stages of this processing for the three Sections analysed in this paper.

The dipmeter data set consists in a series of measurements of depth, azimuth and dip of stratigraphic bedding surfaces (Annex 1). Processing is based on a comparison of changes of bedding attitude at various scales (Figure 1).

A given scale (e.g. 1 m) defines a window size (1 m in this example). For this given scale the data set is cut in successive windows, positioned symmetrically by reference to the center of the depth interval (e.g. eleven windows from 10 to 21 m for a 10.25 - 20.75 m interval). The upper and lower limit of each window define its position. In each window, we compute a best plane, i.e. an average of the bedding plane orientations contained in this window. A change of attitude (tilt) is then calculated between two successive and adjacent windows (Figure 1, Annex 2). Tilt is defined by a rotation axis, a rotation angle, and a tilt way (Annex 2) ; it is located by the position of the limit between the two consecutive windows. As in most cases sedimentary beds are close to the horizontal, the rotation axis are also close to the horizontal, and are defined only by their trends. The tilt way is defined by the azimuth of the lower plane when both upper and lower planes are rotated to bring the upper one horizontal.

Investigation scales vary from the smallest depth-interval between two data (often at centimeter scale), up to the size of the depth interval for the whole data set (few tens to hundred meters). We used a fixed ratio of $10^{0.1}$ between consecutive scales, investigating ten scales between 10 centimeters and 1 meter, between 1 meter and 10 meter, etc.

This first stage of processing results in matrixes of rotation axis trend, rotation angle, and tilt way as a function of depth and window size (Figure 1, Annex 2). Assuming that some changes of orientation represent significative events, and that others represent random noise, the significative events may be identified by constant parameters (axis trend, angle, way) for various and successive window sizes. On the contrary, axis trend and tilt way of noise may vary with window size, and the tilt angle generated by random noise may decrease when stacked in larger depth-windows. The significative events are tracked from the larger to the smaller window sizes, searching similar rotations characterized by significant rotation angles (by default more than 3°), similar axis trend $\pm 20^\circ$) and similar tilt way in the same depth intervals. We retain only as significative events the rotations that can be tracked in at least three successive window sizes (Annex 3). It happens that for a given scale, two successive tilts (i.e. three successive windows) have similar axis trend and tilt way ; in this case we

define the tilt in these three windows by the average trend and by the sum of tilt angles. Among all the rotations tracking a single event for various window sizes, we retain arbitrary the higher rotation angle (Annex 4).

The field example presented in this article has been used to perform several tests for this process :

- Efficiency : does this method correctly identify and measure the sedimentary or structural structures observed on the field ?
- Reproducibility : does this method give similar results when performed in similar sections ?
- Predictive ability : is this method able to identify a structure not observed directly in the logged section, but in its vicinity.

Geological background

The studied sections are located in the Ainsa basin, which represents with Tremp and Jaca basins the Eocene foreland basin south of the Pyrenean belt (Puigdefabregas et al., 1991 ; Figure 2). Lithospheric flexure induced an increasing subsidence towards NorthEast to North-NorthEast. During basin formation and infilling, the development of a thrust ramp (Sierra de Montsec) induced an East-West trending drainage, and the development of the important Sobrarbe delta feeding the Ainsa marine basin from the South East (Figure 2, Dreyer et al., 1999). The propagation of the lateral thrust ramps induced intra-basinal North-South-trending growth anticlines, from East to West, and from the oldest to the youngest : Mediano, Arcusa, Boltana anticlines (Figure 2). These anticlines locally imposed a north-northwestward progradation of the delta. Finally, the Ainsa basin has been unconformably covered by Middle to Upper Eocene continental sediments of Jaca basin (Figure 2).

The studied sections belong to the proximal part of the Sobrarbe delta, at the top of Las Gorgas composite sequence (Dreyer et al., 1999) : the shallower facies are nummulitic limestones, either in situ or resedimented in submarine dunes or sand channels in the delta shoreface ; deeper facies are siltstones and mudstones from the prodelta. In the studied area, the delta front has been affected by large-scale collapses. Dreyer et al. (1999) interpret these collapses as a result of tilting on the flank of a North-South-trending Arcusa growth fold, although they notice that tilting seems to occur towards North-NorthWest. It is noteworthy that the Boltana anticline was not well-developped at the time of deposition of the studied sections, but appeared more recently as a growth fold. Callot et al. (Submitted) identified three sliding surfaces (S1 to S3) in the studied area (Figure 3). S1 and S3 truncate the underlying sediments, with marked angular unconformities (Figures 4 and 5). S1 and S2 are associated to numerous normal faults and clastic dykes that indicate northwestward slides (Callot et al., submitted ; Figure 6). From the orientation of S3 and its vanishing towards north (Figures 3 and 5), a northward slide is postulated for this surface (Callot et al., submitted).

Measurements

We systematically measured available and accessible attitudes of beds along three sections on the right bank of Rio Ena, between barrancos Mazana and Solano (Figure 3 to 5). The measurements were projected horizontally on a vertical log. Elevations are given by reference to the first measure of the section. The error on the difference of depth between two consecutive measures is estimated to 20%, i.e. ± 2 cm for 10 cm, or ± 40 cm for 2 m. As we

measured all observed bed surfaces, measurements are closer in sandstones where individual strata are centimeter- to decimeter-thick, than in mudstones where clear beddings are sparse, and often separated by several meters.

We repeated some measurements ten times to estimate instrumental errors on azimuths and dips. The average standard deviations are 2.5° on azimuth measurements (between 1.25° and 3.34°), and 3.7° on dip measurements (between 2.13° and 5.09°). These errors are clearly smaller than the observed variations of azimuths (more than 30°) and dips (more than 40°).

Section I (Figure 7) is a 74 m-high E-W section located just North of barranco Solano (Figure 3). The two other Sections are located 400 m North of Section I (Figure 3), and define two perpendicular sections across a same hill, N-S and E-W for Sections II and III, respectively (Figures 8 and 9). These two sections are close one to another, and several strata (A to D in Figures 8 and 9) can be correlated between it. Strata E correspond to the same measurements at the top of the hill. The upper parts of Sections II and III are lateral equivalents of the first ten meters above the S3 unconformity located at 47.5 m in Section I.

In these three sections or in their vicinity, we observed several structures associated to changes of bed attitude (Figures 7 to 9): sedimentary structures are mainly cross-bedding in sandstones ; syn-sedimentary or syn-diagenetic normal faults currently occur in mudstones. Some of these structures appears in three dimensions as small-scale sliding scars. In Sections II and III, sedimentary dikes were also observed at the base of A sandstones, following S2 sliding surface (Figure 6). Finally, the large-scale changes of attitude are often associated to pinching-out beds, some of them clearly associated to the main unconformities S1 and S3 identified in the area (Callot et al., submitted) (Figures 4 and 5).

Results

Artifacts

The rigthen parts of Figures 7 to 9 display the significative tilts computed from the variations of bed attitude in Sections I to III, respectively (Annexes 3 and 4). We refer to these rotations by the Section number followed by the tilt number (e.g. I-7). In the three cases, the characteristic scales of identified rotations are of course constrained by the distance between consecutive measurements : in mudstones where bedding are sparse, characteristic scales vary from 1 to 10 meter, while they can be as small as 10 cm in sandstones. With this restriction, the dipmetry logs appear as a succession of tilts at various scales. However, some of these tilts are clearly related one to another. We exemplify these cases in Section I (Figure 7), but they were observed similarly in the two other sections :

- In some cases like I-69 and I-152 (elevation 7 m), or I-193 and I-229 (elevation 24 m), two similar rotations have been identified at different scales but for the same elevations. These double identifications are due to the lack of similar tilt axis for a given window size, inducing an interruption of tilt tracking (Figure 1). However, they correspond to a single tilt event whose location is best indicated by the smallest window size.

- An other peculiar feature occurs when the tilt axis progressively rotates when the window size decreases, such as for I-7, I-13 and I-48 (elevation 24 to 30 m). This indicates a progressive change of preferred orientation with scale : smallest scales (< 1 m) correspond to N-S trending rotation, while large scales correspond to E-W trending rotation.

- Finally, many successive tilts indicate similar rotation axis and angle, but opposite tilt ways (e.g. I-15 and I-124, elevation 2 to 5 m ; I-27 and I-3, elevation 12 to 15 m ; I-10 and I-6, elevation 38 to 46 m). These pairs indicate that two sub-parallel beds enclose oblique beds, as cross-bedding between horizontal beddings (Figure 10A). More generally, it is important to remember that the tilt way does not indicate absolute but relative tilt, by

reference to the upper layer. For instance, depending on the dip of this upper layer at the time of sedimentation, a similar tilt way towards East can be interpreted either as a dune dipping East below an horizontal surface, or as an horizontal surface below a dipping West prograding clinoform (Figure 10B).

Section I : various scales

When taking apart the variations associated to these artifacts, the tilts of Section I can be sorted as follow (Figure 7) :

At scales larger than 25 m, two perpendicular tilts are observed. Both tilt ways indicate eastward dips in the lower part of the section, consistent with the decrease of dip with elevation in the section. However, tilt trends differ between the lower part of the section (I-1, trending N30°) and the upper one (I-2, trending N140°). I-2 rotation indicates a progressive tilt from 46 to 76 m.

At 10-meters scale, we observe three successive tilts : in the lowest interval (below 25 m), two tilts (I-9 and I-3) with similar trend (N160°) but opposite ways ; in the 20-35 m-interval, southward tilt I-7 is E-W-trending ; finally in the upper part of the Section (above 35 m), N140°-trending tilts occur with alternative tilt ways (I-10, I-6, I-2).

At smaller scales, the variability of the intervals between consecutive measurements precludes a description of consecutive tilts. However, we observe only few preferred tilt orientations : in the lowest part of the Section, two consecutive and opposite tilts (I-15 et I-124) trend NE-SW at few meters to few decimeters scales. Elsewhere, N-S trending opposite tilts prevail at the smallest scales, including less than 10 cm-scales. Most of these rotations are first (from bottom to top) eastward tilts, then westward (e.g. I-34, I-152 and I-69 followed upward by I-43, I-9 and I-27). Finally, E-W trending tilt axis appear in the 25 to 48 m interval (e.g. I-63 at 41 m or I-22 at 47 m).

Section I : identifications of structures

At all scales, several identified tilts perfectly fit the structures observed on the field :

In the sandstones, the observed cross-bedding (23, 24, 48 m in Section I) are dune-like structures (Figure 11), with oblique beds dipping East between paleo-horizontal surfaces. These structures fit the identified N-S trending tilts at the same elevations (I-143, I-193 and I-229, I-223, I-204, I-212). Tilts with similar trends are also identified in other sandstone beds where cross-bedding was not directly observed (I-152, I-69, I-43, I-9 in the 7-10 m interval ; I-245 and I-157 in the 25-27 m interval).

At a larger scale, nummulitic limestones are systematically associated to NNW-SSE trending rotations with an ENE tilt way (I-3 at 14 m, I-2 in the uppermost part of Section I).

Finally, pinching out and unconformities are well-identified : S1 and S3 sliding surfaces are similarly identified by E-W-trending tilts (I-49 and I-109, and I-22, respectively), with the underlying beds truncated by a north-dipping unconformity. The same E-W-trending tilt (I-63 at 41 m) is observed associated to pinching out at a smaller scale between the two surfaces. However, small-scale and large-scale pinching out overlying S1 and S3 are mainly characterized by similar NW-SE-trending tilts : tilt I-10 fits the 38-40 m pinching out associated to S1 unconformity, with similar NW-SE trend and tilt way as for rotations I-3 (10-20 m) and I-2 (46-74 m), which represents the large-scale wedge overlying S3 unconformity (Figure 4). I-9 (10 m) and I-6 (45 m) share the same NW-SE axis but with an opposite tilt way.

On the contrary relationships between identified tilts and small-scale paleo-scars are not obvious : the trends of rotation axis do not clearly fit the orientation of sliding surfaces (Figure 7) : I-34 at 6 m trends N25° while the sliding surfaces strike N125° to N-S ; I-72 at 18 m trends N145° while the sliding surfaces strike N-S and N75°. At 24 m, the sliding surfaces

strike N-S, parallel to many N-S trending rotations that can also be attributed to cross-bedding. At 37 m, I-101 trends N-S as sliding surfaces observed laterally.

Sections II and III

In lower parts of Sections II and III (Figures 8 and 9), the large scales (> 7 m) indicate tilts trending NE-SW (II-8 and II-12) and N-S (III-11, III-1 and III-12), respectively. Similar NW-SE-trending tilts occur in the upper parts of both sections (II-13, II-15, II-3 ; III-13, III-8, III-5).

As in Section I, numerous structures observed on the field are directly identified by significative tilts. In the sandstones, tilts in the observed cross-bedding are still trending N-S (III-72 and III-141, III-41 and III-90 in the 11-15 m interval) or NNW-SSE (E strata in Sections II and III). Several tilts fit the location and orientation of the observed small-scale paleo-scars (III-67, III-44 and III-13, III-8 at 22, 26 and 37 m, respectively) or normal faults (III-53 at 1 m), while others (II-15 and II-29, II-24 at 30 and 34 m) are oblique or perpendicular to the orientation of paleo-scars. The sedimentary dykes striking $N40^\circ$ (Figure 6) that underly S2 surface are also well-recorded in both sections (II-44 ; III-26, III-71 and III-88). Finally, the unconformities located at 9 and 11 m (S3) in Section II correspond to E-W-trending tilts (II-45, II-22 and II-37, II-27 and II-38).

As the same data set has been used in the uppermost part of Sections II and III, it represents a good test of the reproducibility of the processing method. Because the position of the investigated windows differs in the two sections, the tracked tilts are not exactly identical. However, both Sections display a similar succession of tilts, for the same strata, with similar trends, angles and tilt ways. Tilt II-119 is the only exception, as it is not observed in Section III, where the change of position of the investigated windows makes the rotation angle too small to be retained.

Interpretation

Dipmetry processing in the three investigated sections shows that this method is able to detect the sedimentary (cross-bedding, unconformity) or tectonic structures (sliding structure, scar, normal fault) observed on the field at various scales. Obviously, this identification provides informations on the geometry of the structures, and allows to discriminate by their orientations structures that can appear comparable on the field. Furthermore, it appears that even when no peculiar structures were observed, the bed attitudes do not vary randomly, but their tilts have preferred orientations that can be ascribed to specific processes identified on other parts of the section. Finally, there are some evidences of reproducibility : in the studied sections we observe similar evolution for two close sections (II and III), especially where the lateral continuity is clear (between strata D and E), but also in the upper part of Section I. Because of shift in the position of investigated windows, there are only slight changes in the results for strata E between Sections II and III.

Of course, dipmetry processing can not be used alone, as it does not provide by itself a geological interpretation of the changes of orientation. But the fact that these changes of orientation are specific to some scales makes the comparison with other data easier. On the field, this method can be time-consuming (for systematic measurements along a section), and lacking precision (because of compass measurements). On the contrary, in drilled borehole, as dipmeter tools provide fast and precise measurements, and moreover allow a systematic survey of bedding attitudes in thicker sedimentary sections, the processing method used herein may be an useful tool to integrate and interpret structural measurements with the other logging records.

For the specific study of the gravity-driven structures in the Sobrarbe delta, the dipmetry results can be interpreted quite simply as a combined effect of sedimentary inputs and large scale tectonic deformations. In the three studied sections as in adjacent places, all evidences, either direct (dunes, cross-bedding, flute-casts) or from dipmetry analysis (N-S-trending tilts in sandstones), indicate a westward transport of detritic particles in this part of the delta. There are only small-scale evidences of N-S-trending gravity-driven sliding, that were probably controlled by sedimentary overloading. These sediments deposited north of the northern termination of the N-S-trending Arcusa anticline, and west of northern termination of Mediano anticline (Dreyer et al., 1999 ; Figure 12). While detrital displacement was controlled southward by the N-S-trending Mediano and Arcusa anticlines, the westward transport in the studied area probably indicates a change of orientation of the transport network where the Arcusa anticline disappears (Figure 12). An alternative hypothesis can be an independant detrital network coming from the uplifted westernmost part of Tremp basin (Figure 5 in Dreyer et al., 1999), crossing the northern termination of Mediano anticline, and converging with the main delta north of Arcusa anticline (Figure 12).

The large scale tectonic deformations are best indicated by E-W-trending tilt axis, associated to S1 and S3 unconformities in Sections I and II. These tilts can be interpreted either as resulting from the regional northward tilt of the flexural basin, or more probably as the southward uplift of the growing Arcusa anticline (Figure 12). In both cases, the recorded tilts in the studied sections are by several orders larger than the large-scale tilt : these mechanisms can only trigger gravity-driven instabilities, inducing locally steep slopes.

A combination of this northward regional tilt with a westward sedimentary transport may generate a NE-SW striking slope at the edge of the delta. This NE-SW direction is mainly recorded by large scale tilts in the lower parts of Sections I and II, but also by extensional structures (normal faults, some small-scale scars, sedimentary dykes), especially associated to sliding surface S2 in Sections II and III (Figure 12).

Finally, it has been observed a significative, while not systematic, difference between tilt axis trend and scar strikes. As proposed by Callot et al. (submitted), this difference may be due to the curvature of slump scar. The arcuate fault may range from perpendicular to the sliding displacement (in the center) to parallel to it (on the edges). A good example is given by the structures observed at 30 m in Section II (Figure 8), where normal faults accommodates a WNW-ESE extension, but where the overlying sliding scars observed just above strike E-W, and probably represent the edge of an arcuate structure. In this case as at larger scale in the upper part of the three Sections, the associated NNW-SSE-trending tilt axis can represent the structures associated to the edge of NNW-SSE elongated sliding surfaces S1 and S3 (Figure 12). Furthermore, the large-scale NNW-SSE-trending tilt associated with nummulitic limestones in Section I, and its ENE tilt way can be interpreted as the record of the southwestward progradation of the overlying mudstones, infilling from the side the depressions formed by previous glidings.

Conclusions

While needing a careful interpretation, the proposed processing method appeared to be successful on this field test in identifying the structures, quantifying the associated tilts and characteristic scales. Easier applications of this processing method can be expected from dipmetry logging in boreholes, even if the geological interpretation will need in every case an integration of all available data. For gravity-driven slides, this method can be helpful, as tilt

trends can be expected to be close to the perpendicular of the slide directions, while fault strikes can not easily be related to displacements in arcuate structures.

In the studied area, the variations of orientation of the sedimentary beds can be interpreted as resulting from a sedimentary input from east to west, regional tilts towards North triggering the main gravitational instabilities, and a NE-SW local submarine slope.

Acknowledgments

This work has been funded by the french Groupes De Recherche Marges and Corinthe. We thank our colleagues from the GDR Marges group ‘gravity instabilities’, especially for discussions during the Toulouse workshop in 2004.

References

- Basile, C., 2000. Late Jurassic sedimentation and deformation in the west Iberia continental margin : insights from FMS data, ODP Leg 173. *Marine and Petroleum Geology*, 17, 709-721.
- Bengtson, C. A., 1981. Statistical curvature analysis techniques for structural interpretation of dipmeter data. *American Association of Petroleum Geologists Bulletin*, 65, 312-332.
- Berg, C. R., 1998. Synthetic deviation : a new dipmeter interpretation method. *American Association of Petroleum Geologists Bulletin*, 82, 6, 1133-1139.
- Callot, P., Odonne, F., Debroas, E. J., Maillard, A., Dhont, D., Hoareau, G., submitted (April 2006). 3D architecture of Eocene submarine slide scars in the Sobrarbe area (Ainsa, Spanish Pyrenees). *Sedimentology*.
- Donselaar, M.E., Schmidt, J.M., 2005. Integration of outcrop and borehole image logs for high-resolution facies interpretation : example from a fluvial fan in the Ebro Basin, Spain. *Sedimentology*, 52, 1021-1042.
- Dreyer, T., Corregidor, J., Arbues, P., Puigdefabregas, C., 1999. Architecture of the tectonically influenced Sobrarbe deltaic complex in the Ainsa Basin, northern Spain. *Sedimentary Geology*, 127, 3-4, 127-169.
- Fernández Bellon, O., 2004. Reconstruction of geological structures in 3D : an example from the southern Pyrenees. Ph-D Thesis, Universitat de Barcelona, 317 p.
- Gilreath, J.A., 1987. Dipmeter interpretation rules – part 1. *The Technical Review*, 35, 3, 28-41.
- Hesthammer, J., Fossen, H., 1998. The use of dipmeter data to constrain the structural geology of the Gullfaks Field, northern North Sea. *Marine and Petroleum Geology*, 15, 549-573.
- Höcker, C., Eastwood, K. M., Herweijer, J. C., Adams, J. T., 1990. Use of dipmeter data in clastic sedimentological studies. *American Association of Petroleum Geologists Bulletin*, 74, 2, 105-118.

Hurley, N. F., 1994. Recognition of faults, unconformities, and sequence boundaries using cumulative dip plots. American Association of Petroleum Geologists Bulletin, 78, 8, 1173-1185.

Luthi, S. M., Banavar, J. R., 1988. Application of borehole images to three-dimensional geometric modeling of eolian sandstone reservoirs, Permian Rotliegende, North Sea. American Association of Petroleum Geologists Bulletin, 72, 9, 1074-1089.

Puigdefabregas, C., Muñoz, J. A., Verges, J., 1991. Thrusting and foreland basin evolution in the southern Pyrenees. In : McClay, K. (Ed.), Thrust tectonics. Chapman and Hall, London, pp. 247-254.

Serra, O., 1989. Formation MicroScanner image interpretation. Schlumberger Educational Services, Houston, 117 p.

Figure captions

Figure 1 : Successive steps of dipmetry processing : data set, computing tilts as a function of scale, identifying significative tilts. Stereographic projections : Wulff nets, lower hemisphere. See text for details. Tilts and tracked tilts are shown as in Figures 7 to 9.

Figure 2 : Simplified geological map of the central part of the spanish Eocene foreland basin (modified from Fernández Bellon, 2004). The box locates Figure 3.

Figure 3 : Location of studied Sections I to III (Figures 4, 5, 7 to 9) and main sliding structures (S1 to S3, according to Callot et al., submitted). S1 and S3 in grey where hidden. Elevation in meters.

Figure 4 : Section I outcrop, located Figure 3. Measurements follow the dashed line ; the lowest part of the section is not visible on this picture. The main sliding surfaces S1 and S3 are underlined, together with stratigraphic markers α and β (Figure 7). View to the south east.

Figure 5 : Sections II and III outcrop, located Figure 3. Measurements follow the dashed line. The main sliding surfaces S2 and S3 are underlined, together with some stratigraphic markers (A, C to E, Figures 8 and 9). Notice the changes of thickness between D and E. View to the north, Boltana anticline in the background.

Figure 6 : Sedimentary dykes in the mudstones below sandstones A and sliding surface S2 (located in Sections II and III, Figures 8 and 9). Stereographic projection (Wulff net, lower hemisphere) of the dykes measured in the same stratigraphic layer. Notebook (17.5 x 11.5 cm) for scale. Location Figure 5.

Figure 7 : Sedimentary and dipmeter (dip direction and dip) logs for Section I. Strata α and β and sliding surfaces S1 and S3 are located on Figure 4 ; S1 and S3 are also mapped on Figure 3. The lateral equivalent of the upper part of Sections II (above S3) and III (above layer C) is located above S3 surface. On the right part, tilt tracking (grey lines) as a function of investigated window size, and identified significative tilts from processing of dipmeter data

(cf. text and Figure 1). Tilts are referenced by a number attributed during tracking. They are referenced in the text by the Section number and the tilt number (e.g. I-7) ; circled numbers exemplify the structures drawn in Figure 12. Stereographic projections : Wulff nets, lower hemisphere.

Figure 8 : Section II. A to E are common stratigraphic markers in Sections II and III. Strata A and C to E and sliding surfaces S2 and S3 are located on Figure 5 ; S2 and S3 are also mapped on Figure 3. Same caption as for Figure 7.

Figure 9 : Section III. A to E are common stratigraphic markers in Sections II and III. Strata A and C to E and sliding surface S2 are located on Figure 5 ; S2 and S3 are also mapped on Figure 3. Same caption as for Figure 7.

Figure 10. 10A : A single sedimentary structure may be identified by two tilts with opposite tilt ways. Tilt symbol as in Figure 7 to 9. 10B : Various interpretations of the same tilt : the tilt way does not give indications on sedimentary surfaces intersection ; the same tilt way can correspond either to downlap or toplap, but also to curved surfaces.

Figure 11 : Submarine dune built by an accumulation of Nummulites (white dots). Lateral equivalent of sandstones, elevation 48 m, Section I (Figure 7). Compass for scale (9 x 10 cm). Location Figure 4.

Figure 12 : Schematic 3-D view of the main types of structures observed and deduced from dipmeter logs. Numbers refer to examples of tilts associated to each type of structure.

Annexes

Annex 1 : Dipmetry measures (dip direction, dip, elevation) for Sections I to III.

Annex 2 : Computed tilts for Sections I to III.

Annex 3 : Significant tilts (displayed as paths in Figures 7 to 9) for Sections I to III.

Annex 4 : Retained tilts (displayed in Figures 7 to 9) for Sections I to III.

Figure 1 Data set

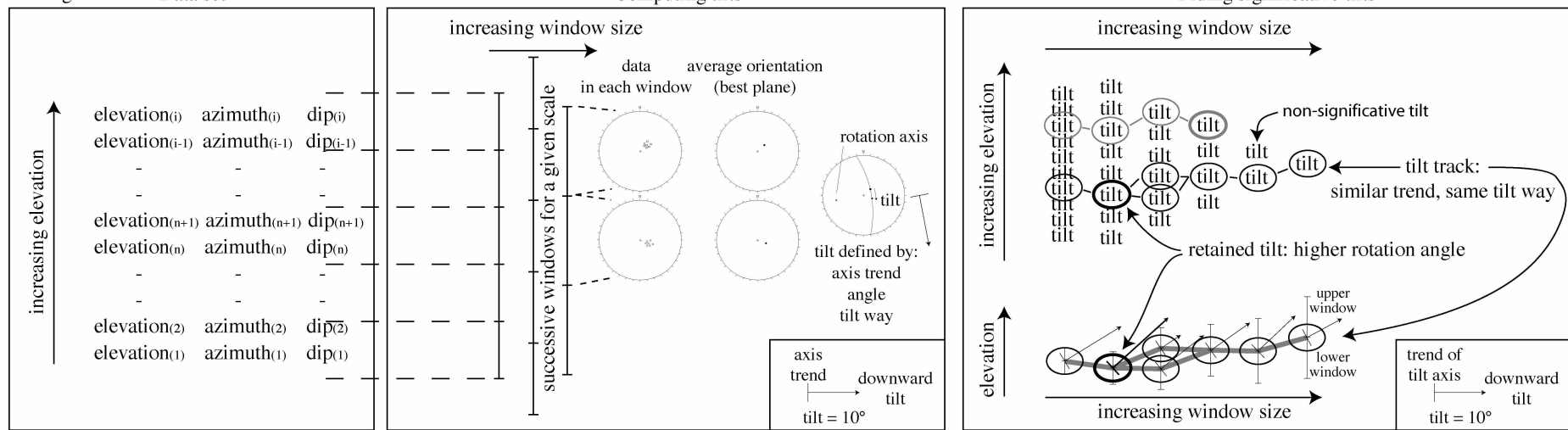


Figure 2

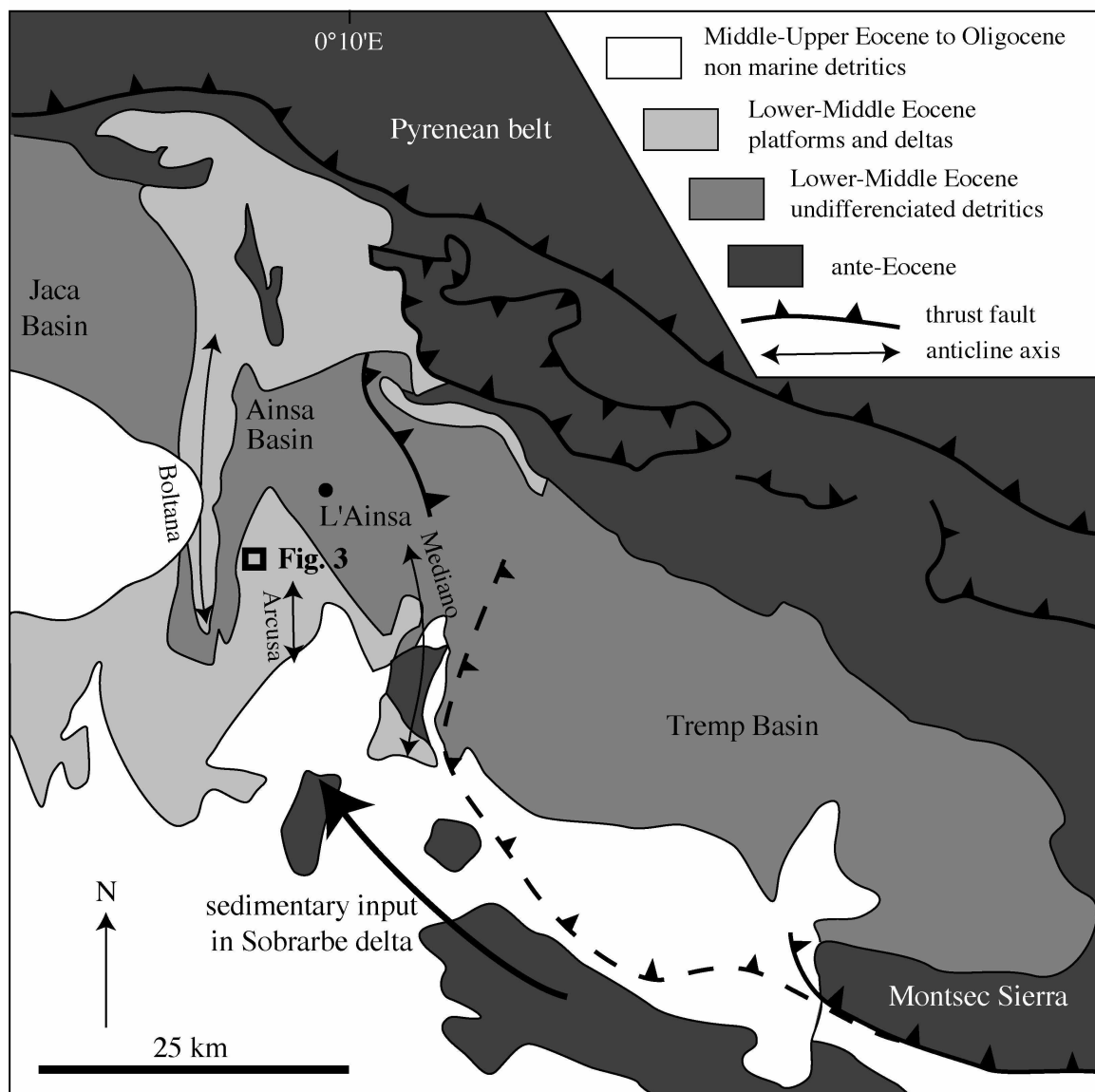


Figure 3

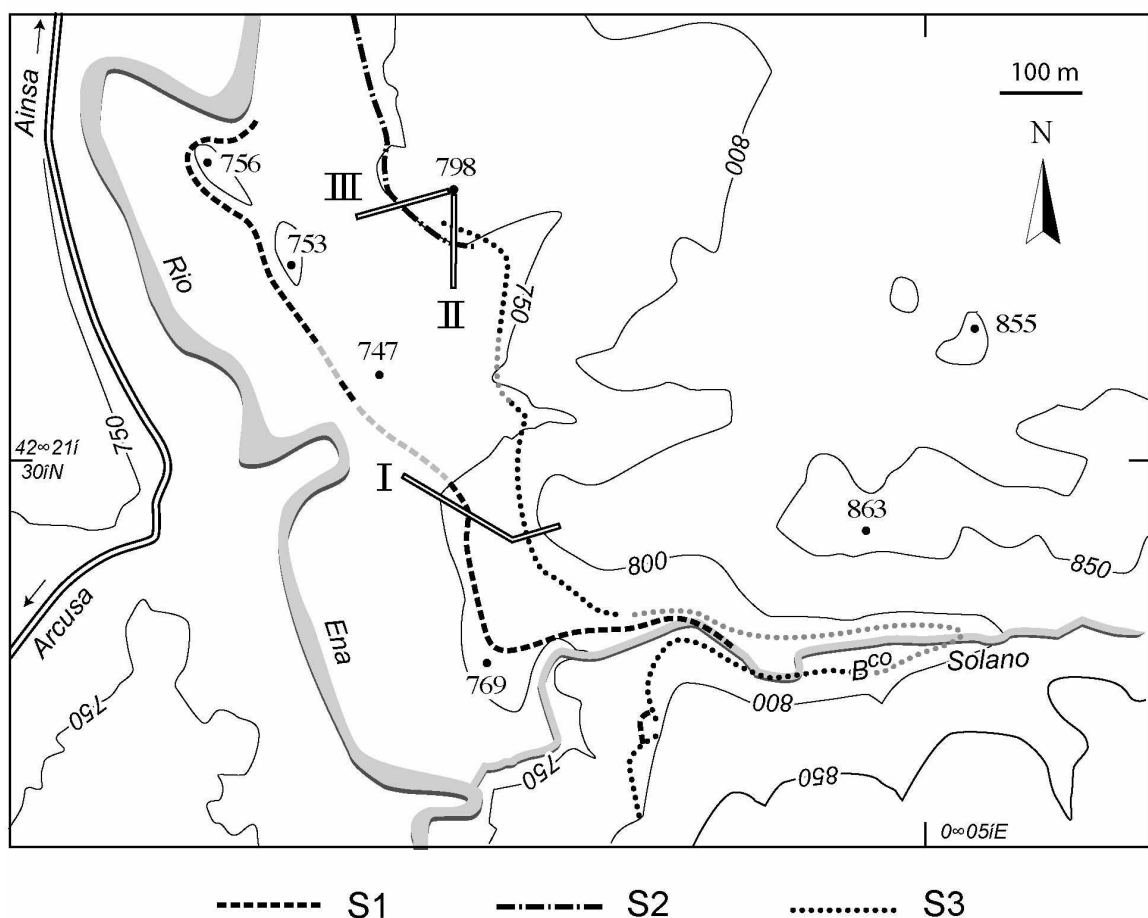


Figure 4



Figure 5



Figure 6

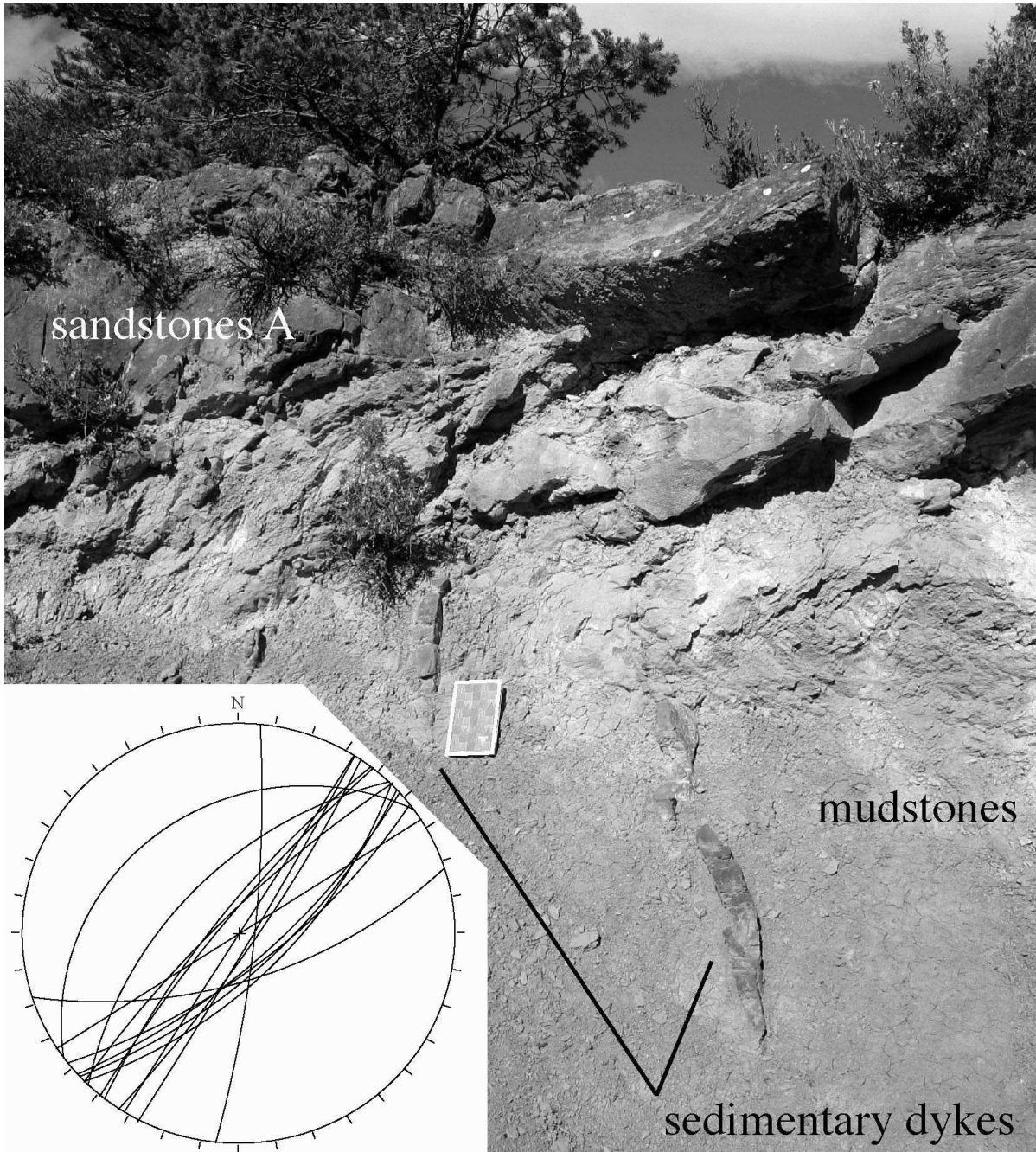


Figure 7

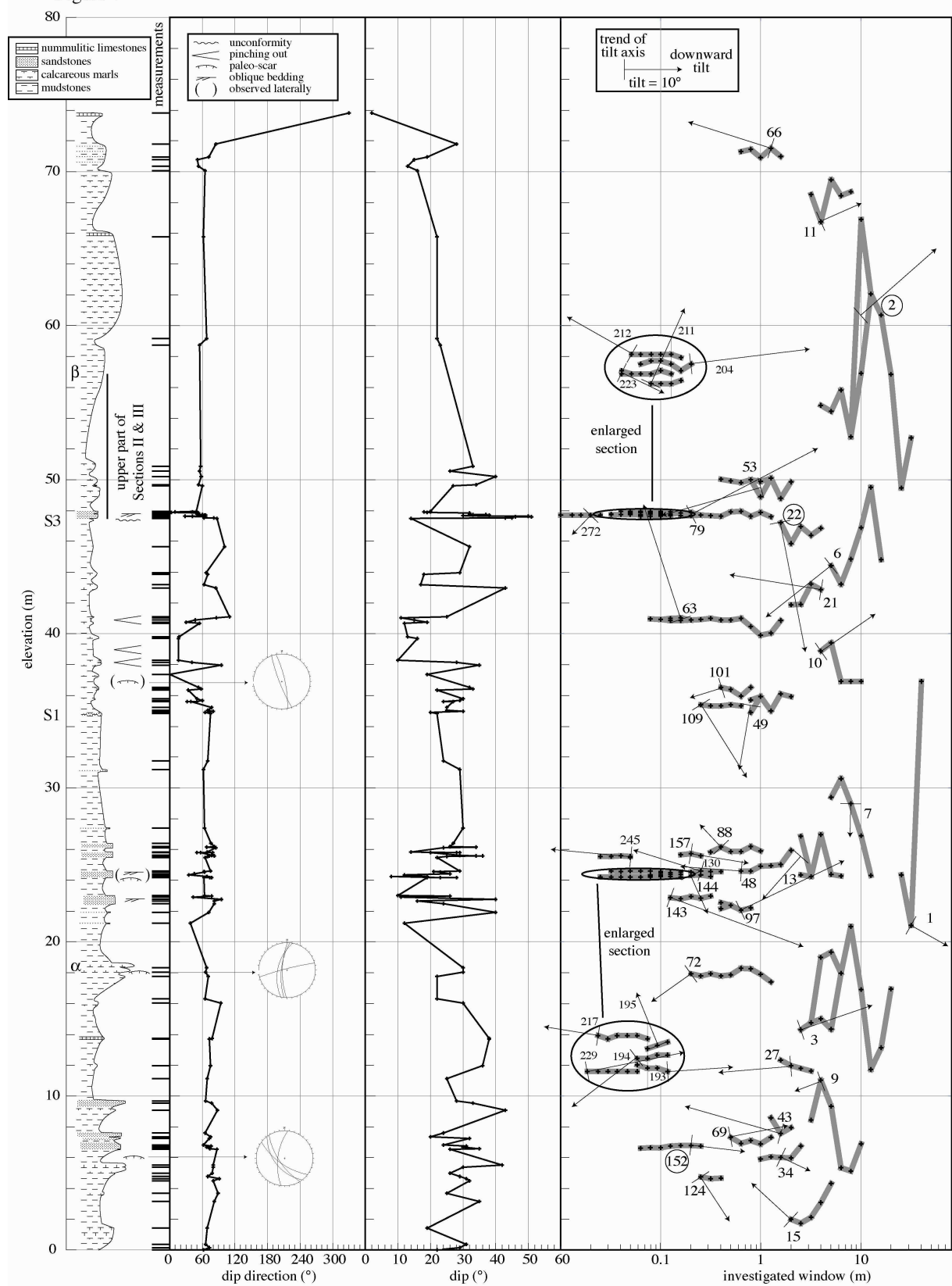
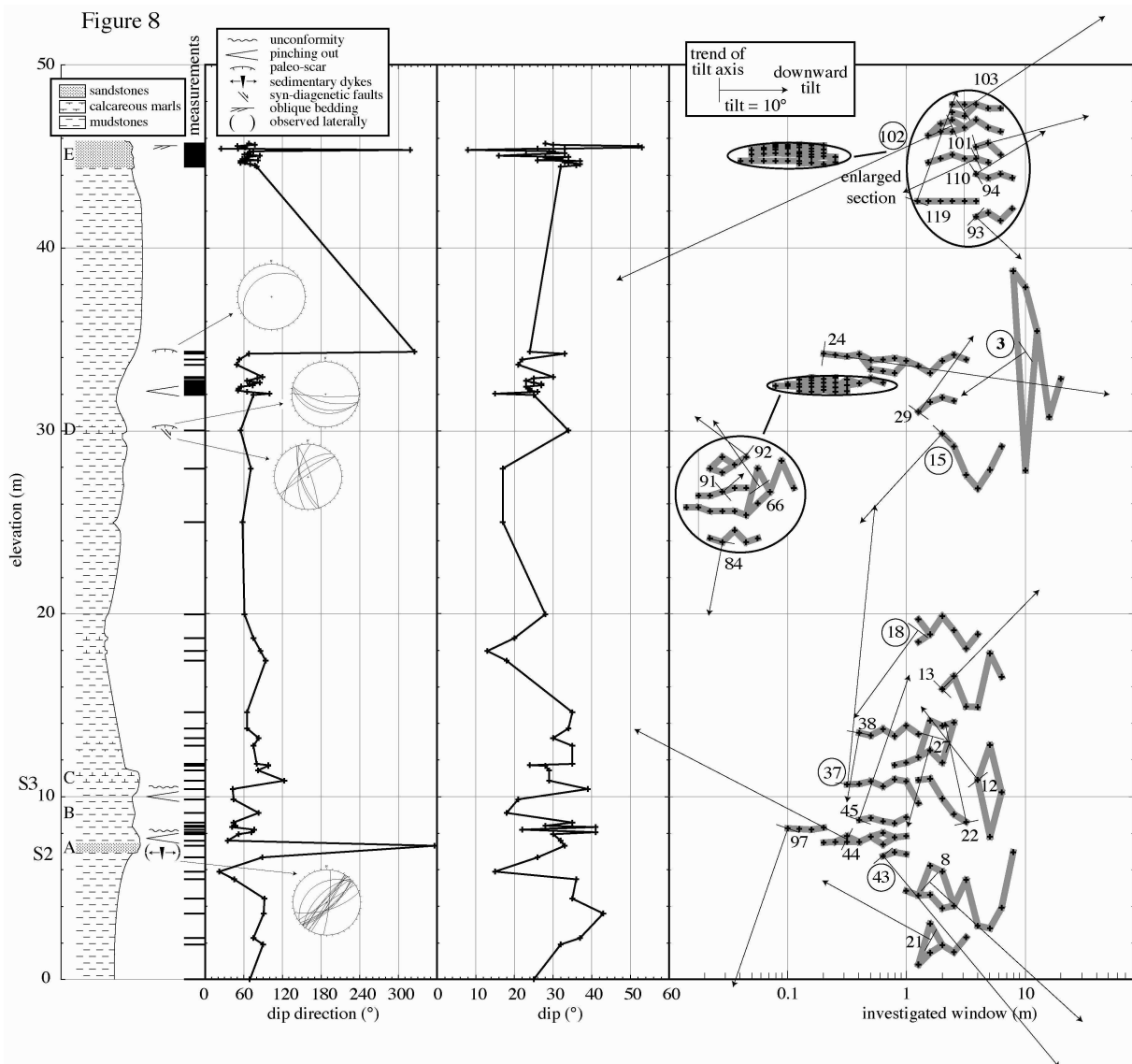


Figure 8



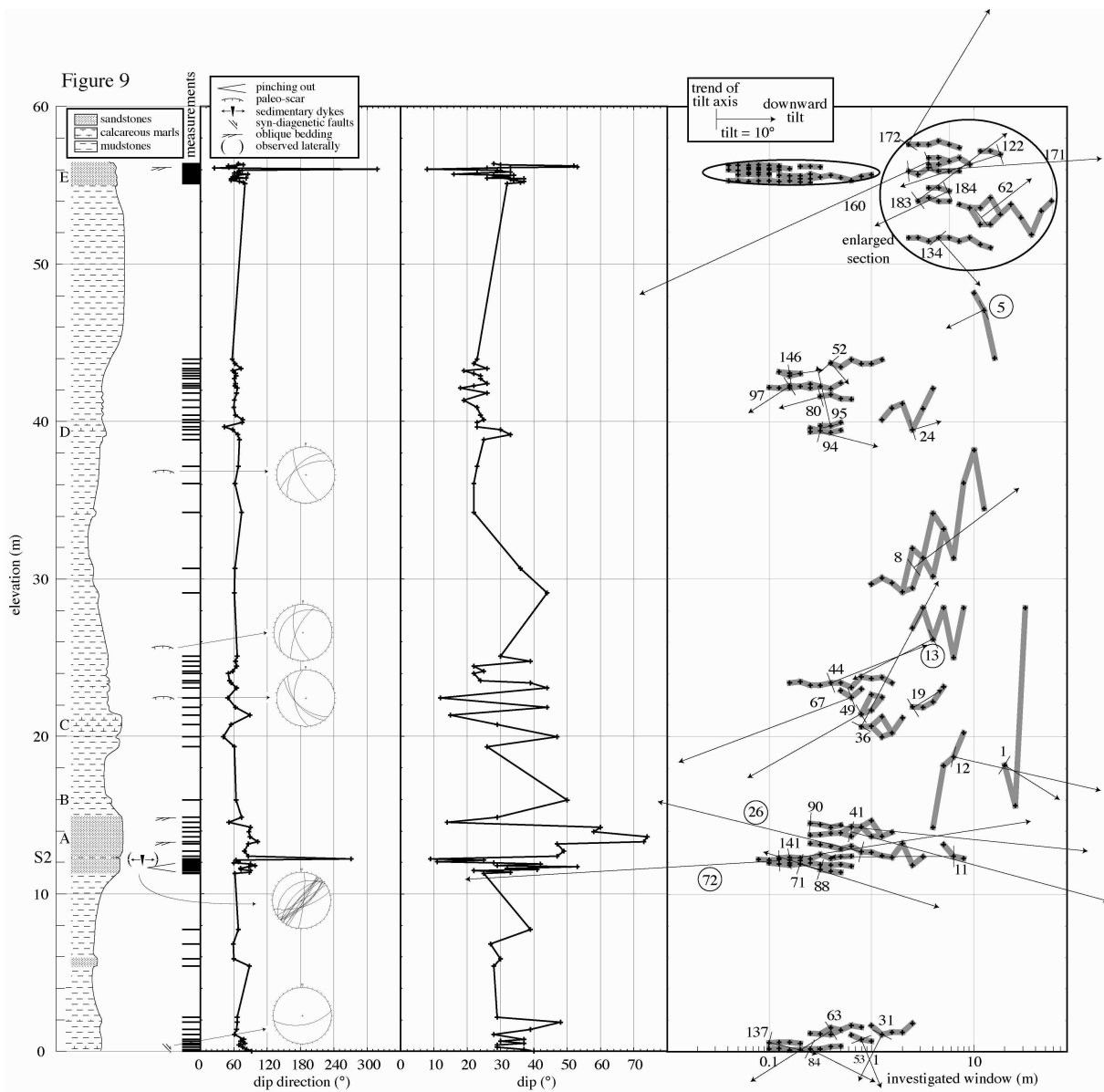


Figure 10

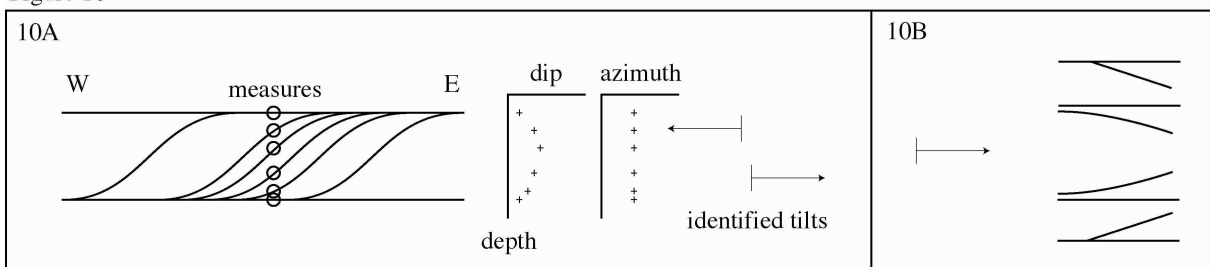


Figure 11

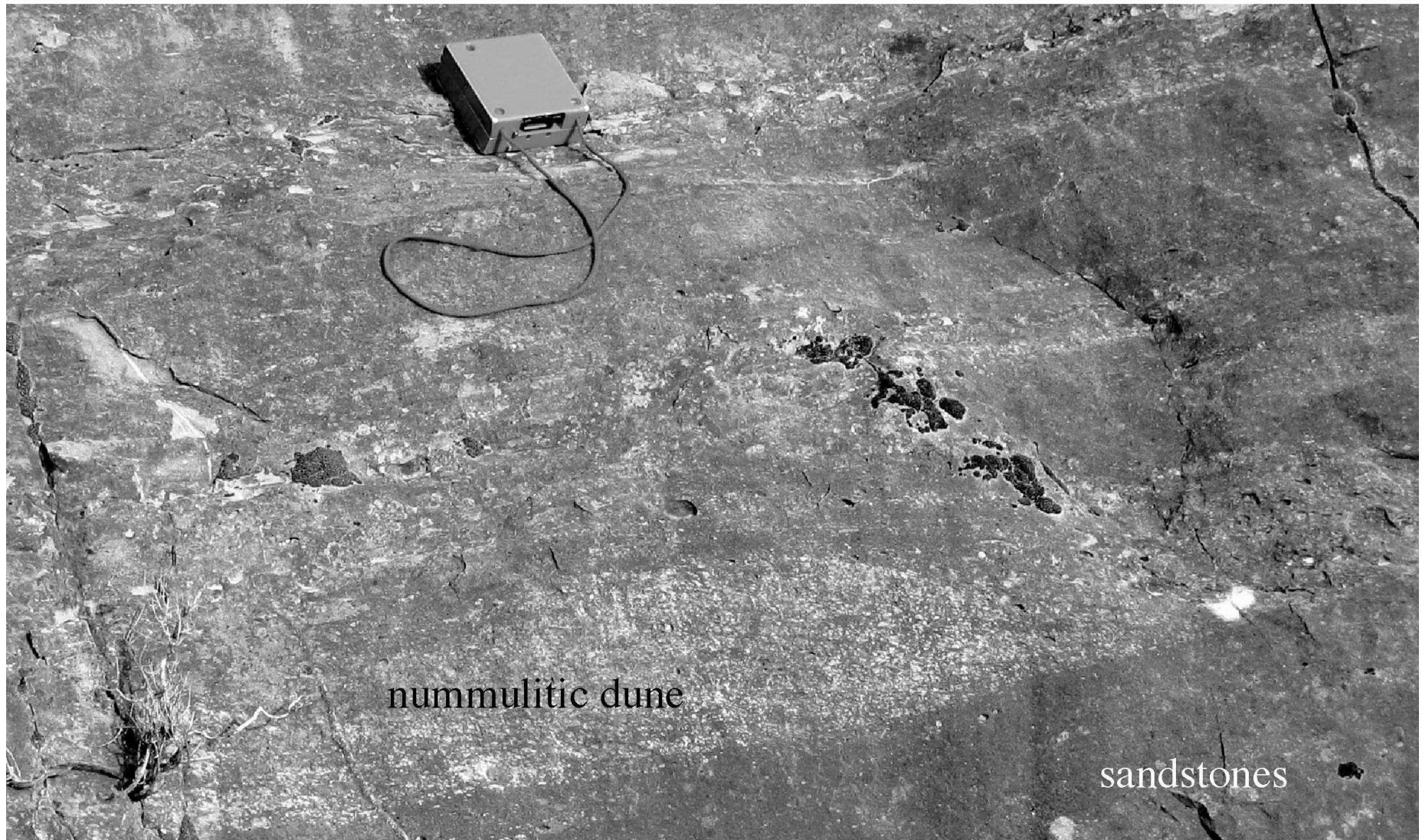
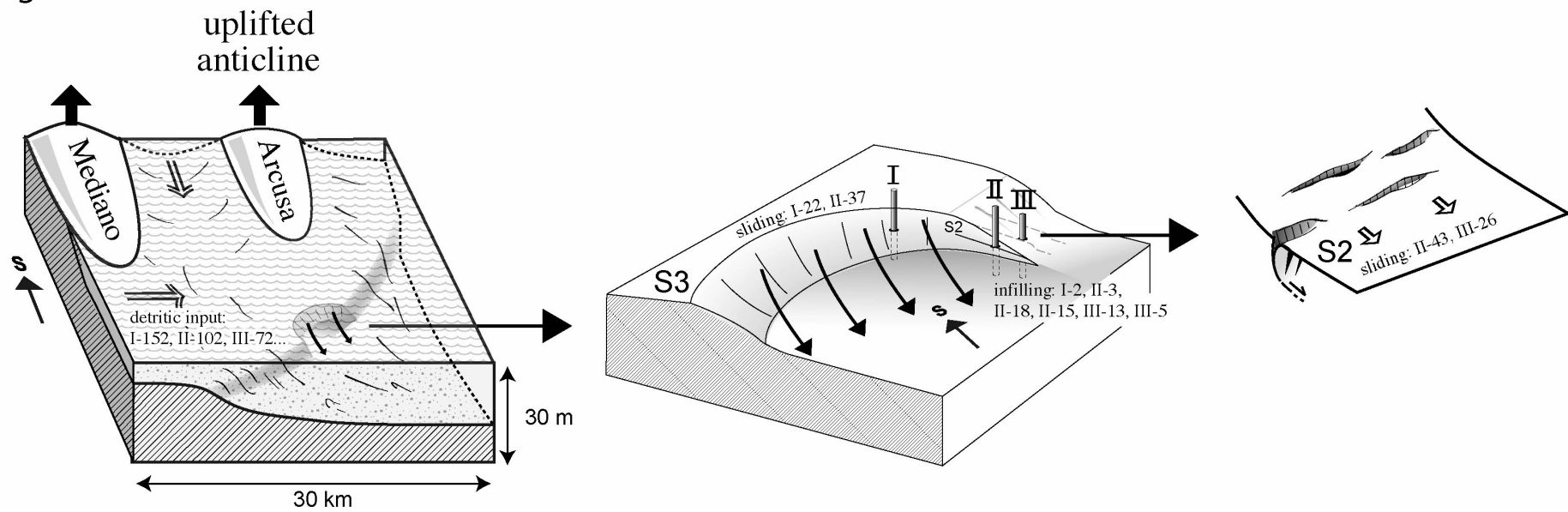


Figure 12



Annex 1

Section I

dip direction	dip	elevation
62	22	0
73	29	0.1433725
66	31	0.35843125
69	19	1.433725
82	35	3.154195
89	25	3.670336
80	32	4.5018965
91	31	4.645269
70	29	4.7886415
78	26	4.989363
80	30	5.3621315
80	42	5.505504
87	26	6.537786
74	35	6.595135
68	30	6.6811585
76	31	6.75284475
62	24	6.81019375
73	32	7.24031125
75	20	7.35500925
65	24	7.58440525
88	43	9.07547925
77	33	9.53427125
66	28	9.67764375
69	25	11.11136875
75	36	11.97160375
73	38	13.69207375
78	38	13.74942275
94	30	16.04338275
65	22	16.33012775
71	22	17.76385275
66	30	18.05059775
68	30	18.33734275
38	12	21.20479275
72	40	21.92165525
82	24	22.49514525
82	16	22.66719225
95	40	22.75321575
43	11	22.89655825
77	26	22.98261175
64	10	23.0256235
63	19	24.1726035
77	28	24.1898082
74	23	24.1955431
68	8	24.23855485
69	19	24.26722935
35	12	24.35325285
45	26	24.41060185
64	23	24.52529985
63	21	24.58264885
75	29	24.61132335
65	22	25.47155835
70	25	25.55758185
73	36	25.58625635
82	34	25.59772615
77	29	25.61493085
57	20	25.78697785
50	28	25.79271275
79	29	25.81565235
69	14	25.8299896
85	24	26.1167346
68	34	26.151144
82	26	26.1740836
76	27	26.4034796
64	30	27.39274985
62	29	31.20645835
70	24	31.77994835
75	22	34.81944535
65	20	34.90546885
80	30	34.96281785
70	25	35.04884135
77	25	35.22088835
39	27	35.59365685
32	24	35.6022592
50	24	35.61086155
60	29	35.66247565
50	30	35.77717365
34	22	36.35066365
58	33	36.40801265
53	32	36.52271065
0	19	37.38294565
95	35	37.95643565
41	28	38.1428199
16	10	38.30052965
16	16	39.6969778
17	13	39.79733855
55	12	40.7005853
30	19	40.7579343
47	15	40.9013068
86	11	41.03034205
110	25	41.11636555
85	43	42.98020805
63	17	43.20960405
70	18	43.86911755
67	29	43.95514105
101	32	45.67561105
87	14	47.51077905
81	45	47.53945355
63	43	47.5480559
66	46	47.58533275

63	51	47.59680255
28	50	47.62547705
42	38	47.6398143
64	30	47.67135625
66	38	47.6971633
65	33	47.71150055
64	37	47.7201029
60	37	47.73444015
55	33	47.74017505
50	32	47.7774519
53	32	47.8348009
3	19	47.8921499
42	18	47.9036197
10	20	47.92369185
49	20	47.9667036
60	27	49.61548735
53	34	49.6871736
58	40	50.2033146
55	26	50.56174585
57	33	50.8915026
55	23	58.7483156
68	22	59.1784331
62	22	65.7735681
65	16	70.0747431
53	13	70.3614881
51	15	70.7916056
72	19	70.9349781
85	28	71.7952131
330	2	73.8024281

Section II

dip direction	dip	elevation
69	25	0
90	32	1.91
75	37	2.26
91	43	3.62
92	35	4.44
45	36	5.47
22	15	5.89
89	26	6.69
356	33	7.32
35	32	7.6
52	30	7.95
72	41	8.07
76	22	8.19
42	41	8.34
47	28	8.42
44	35	8.58
83	18	9.11
44	21	9.85
43	39	10.41
123	29	10.89
82	29	11.44
98	28	11.68
98	24	11.73
80	35	11.78
75	35	12.79
83	30	13.19
65	34	13.72
65	35	14.63
94	18	17.43
86	13	17.95
75	20	18.68
61	28	19.98
58	17	25
71	17	27.95
55	34	30.04
75	25	31.97
100	15	32.05
65	26	32.13
51	24	32.21
52	24	32.33
56	23	32.41
74	27	32.49
69	27	32.57
85	25	32.65
65	23	32.73
81	25	32.88
89	30	32.96
49	21	33.62
53	22	33.92
68	33	34.22
325	24	34.32
80	32	44.46
77	36	44.53
70	37	44.59
55	34	44.65
62	33	44.71
55	37	44.77
82	26	44.8
58	32	44.87
65	28	44.93
66	34	44.99
85	16	45.05
61	23	45.11
68	33	45.18
69	29	45.24
75	30	45.3
318	8	45.36
25	26	45.42
51	33	45.45
62	53	45.52

50	52	45.58
77	30	45.64
68	28	45.7

Section III

dip direction	dip	elevation
92	40	0
83	37	0.13
76	29	0.26
69	29	0.39
80	37	0.52
72	30	0.65
78	37	0.77
61	28	1.08
65	39	1.39
66	48	1.86
66	29	2.17
88	28	5.42
60	30	5.89
59	27	6.81
68	39	7.74
62	25	11.31
88	33	11.39
90	22	11.47
73	41	11.56
72	32	11.64
87	53	11.73
98	29	11.81
90	42	11.89
60	28	11.98
68	11	12.06
64	25	12.15
271	9	12.23
86	47	12.39
79	49	12.7
86	47	13.16
103	73	13.32
89	74	13.63
87	58	13.94
90	60	14.25
51	14	14.56
74	29	14.87
64	50	15.95
61	26	19.36
41	47	19.98
55	29	20.75
89	15	21.37
63	44	21.84
49	12	22.46
65	44	23.08
55	39	23.39
52	24	23.54
50	22	24
58	25	24.16
65	22	24.47
63	39	24.78
66	30	25.09
61	44	29.12
62	36	30.66
74	22	34.23
62	22	36.08
68	23	37.17
70	25	38.87
67	33	39.18
58	30	39.49
43	23	39.65
75	23	39.96
76	25	40.11
63	24	40.42
60	23	40.89
61	19	41.35
65	26	41.81
66	18	42.12
62	22	42.28
63	26	42.43
61	24	42.74
64	24	42.9
63	22	43.05
58	19	43.21
73	26	43.36
62	22	43.67
57	23	43.98
80	32	55.13
77	36	55.2
70	37	55.26
55	34	55.32
62	33	55.38
55	37	55.44
82	26	55.47
58	32	55.54
65	28	55.6
66	34	55.66
85	16	55.72
61	23	55.78
68	33	55.85
69	29	55.91
75	30	55.97
318	8	56.03
25	26	56.09
51	33	56.12
62	53	56.19
50	52	56.25

77	30	56.31
68	28	56.37

122	0.251	56.200	10.050	178.100	271.682
122	0.200	56.220	12.510	8.000	281.351
134	0.251	55.190	9.400	94.400	182.364
134	0.200	55.230	8.940	74.400	164.993
134	0.158	55.290	9.580	52.100	146.153
134	0.126	55.260	8.470	57.500	150.960
134	0.100	55.290	9.080	43.000	138.791
134	0.079	55.280	10.890	48.600	143.342
134	0.063	55.260	8.300	63.700	156.411
134	0.050	55.280	9.190	39.700	134.979
134	0.040	55.280	9.190	39.700	134.979
137	0.200	0.560	3.300	9.100	102.936
137	0.158	0.610	4.460	19.900	115.876
137	0.126	0.620	8.260	13.800	108.958
137	0.100	0.590	8.260	13.800	108.958
141	0.200	12.130	11.060	161.600	72.159
141	0.158	12.020	16.930	178.700	90.980
141	0.158	12.180	26.380	163.600	74.013
141	0.126	12.200	33.250	160.800	71.441
141	0.100	12.190	33.250	160.800	71.441
141	0.079	12.220	33.250	160.800	71.441
146	0.200	43.050	4.460	175.600	87.185
146	0.158	42.930	2.040	163.700	74.595
146	0.158	43.090	3.470	179.200	90.947
146	0.126	43.170	3.470	179.200	90.947
160	0.158	56.080	22.800	134.900	224.497
160	0.126	56.140	34.800	155.000	246.651
160	0.100	56.090	34.100	162.400	253.175
160	0.079	56.070	28.700	144.100	234.006
160	0.079	56.150	27.980	166.500	260.273
160	0.063	56.080	28.700	144.100	234.006
160	0.063	56.140	27.980	166.500	260.273
171	0.126	56.010	18.900	21.700	115.525
171	0.100	55.990	25.640	10.500	103.940
171	0.079	55.990	34.310	176.100	87.709
171	0.063	56.020	34.310	176.100	87.709
171	0.050	55.980	34.310	176.100	87.709
171	0.040	56.000	34.310	176.100	87.709
172	0.126	56.260	25.630	134.400	37.366
172	0.100	56.290	27.050	124.600	25.900
172	0.079	56.310	27.050	124.600	25.900
172	0.063	56.270	27.840	121.100	20.920
172	0.050	56.280	27.840	121.100	20.920
172	0.040	56.280	27.840	121.100	20.920
183	0.100	55.690	12.090	148.300	57.057
183	0.079	55.670	16.700	139.400	46.835
183	0.063	55.700	19.500	143.000	50.403
183	0.050	55.680	19.500	143.000	50.403
184	0.100	55.790	13.940	154.700	244.339
184	0.079	55.830	8.670	175.500	267.452
184	0.063	55.830	10.510	170.800	262.338

Section I

Tilt number	window size	depth	tilt angle	tilt axis	tilt way
1	31.623	21.09	7.19	29.4	123.183 7.19 7.19
2	10	56.9	10.28	135.4	43.511 15.63 #REF!
2	10	66.9	7.66	141.9	51.111 17.94 ####
3	3.162	14.77	13.3	161.1	69.964 13.3 #REF!
6	5.012	44.42	14.65	141.6	231.125 14.65 #REF!
7	7.943	28.96	5.55	91.1	179.37 5.55 #REF!
9	3.981	11.03	4.58	159.3	248.675 4.58 #REF!
10	3.981	38.9	11.5	145.4	55.566 11.5 #REF!
11	3.981	66.76	7.61	156.2	66.495 7.61 #REF!
13	2.512	24.35	4.31	129.5	217.556 7.15 #REF!
13	2.512	26.86	5.51	133.5	221.218 9.82 ####
15	1.995	1.99	9.26	42.7	314.668 9.26 #REF!
21	3.981	42.88	16.44	9.2	279.875 16.44 16.44
22	1.585	47.21	23.69	79	172.171 23.69 #REF!
27	1.995	11.96	12.73	175.1	266.593 12.73 #REF!
34	1.585	6	5.33	25.2	119.924 5.33 #REF!
43	1.585	7.58	17.69	15.9	289.201 17.69 #REF!
48	0.631	24.6	10.63	4.2	275.739 10.63 #REF!
49	0.794	34.92	6.18	111.2	199.68 8.6 #REF!
49	0.794	35.71	5.27	88.3	175.407 11.45 ####
53	1	48.9	15.76	174.8	266.029 15.76 #REF!
53	1	49.9	2.57	153.7	245.999 18.33 ####
63	0.158	40.87	6.34	78.4	346.753 16.49 #REF!
63	0.158	41.03	15.27	65.5	334.822 21.61 ####
66	1.259	71.53	15.35	17.6	288.467 15.35 #REF!
69	0.501	7.33	10.19	169.2	80.167 10.19 #REF!
72	0.2	17.95	8.29	144.6	233.404 8.29 #REF!
79	0.2	47.68	4.22	151.8	61.913 19.22 #REF!
79	0.2	47.88	21.42	173	87.433 25.64 ####
88	0.398	26.16	5.09	46.8	317.645 5.09 #REF!
97	0.631	22.08	20.55	154.5	62.26 20.55 #REF!
101	0.398	36.51	5.51	162.8	255.205 5.51 #REF!
109	0.251	35.4	15.25	57.9	149.54 15.25 #REF!
124	0.251	4.75	9.08	56.7	150.415 9.08 #REF!
130	0.251	24.6	12.44	17.3	289.174 12.44 #REF!
143	0.126	22.87	25.45	20.3	114.716 25.45 #REF!
144	0.2	24.33	7.07	66	156.092 7.07 #REF!
152	0.2	6.78	9.39	6.8	100.481 9.39 #REF!
157	0.2	25.73	10.16	9.3	102.872 10.16 #REF!
193	0.158	24.23	11.43	176.1	87.295 11.43 #REF!
194	0.079	24.35	14.32	142.6	232.919 14.32 #REF!
195	0.126	24.5	9.87	67.7	335.755 9.87 #REF!
204	0.158	47.84	21.42	173	87.433 21.42 #REF!
211	0.063	47.63	14.54	114.1	15.258 14.54 #REF!
212	0.04	47.95	13.11	29.5	298.406 13.11 #REF!
217	0.032	24.59	9.44	9.1	280.942 9.44 #REF!
223	0.032	47.74	5.19	23.4	119.39 6.76 #REF!
223	0.032	47.77	2.87	28.7	122.486 8.06 ####
229	0.032	24.21	17.59	168.8	79.09 17.59 #REF!
245	0.05	25.5	3.6	8.9	280.921 3.6 #REF!
245	0.05	25.55	10.56	1.7	273.733 14.16 ####
272	0.02	47.72	4.34	134	220.485 4.34 #REF!

Section II

Tilt number	window size	depth	tilt angle	tilt axis	tilt way
3	10	27.85	3.94	140.3	229.734
3	10	37.85	7.56	150.6	240.241
8	1.585	4.63	30.37	36.8	133.872
8	1.585	6.21	1.2	48	136.255
12	3.981	10.91	13.81	52.2	322.156
13	1.995	15.87	20.92	134.3	40.192
15	1.995	29.84	18.2	132.5	221.43
18	1.259	18.45	6.54	127.6	216.393
18	1.259	19.71	9.77	124.7	212.984
21	1.585	1.46	11.24	16.8	289.483
21	1.585	3.04	7.34	40.5	316.237
22	3.162	8.62	15.41	77.9	344.907
24	0.2	34.23	44.25	8.1	102.609
27	1.585	12.55	8.49	113.5	200.845
27	1.585	14.14	5.49	97.3	183.884
29	1.259	31.04	13.99	125.6	32.064
37	0.316	10.68	42.89	95.6	358.449
38	0.398	13.5	10.3	100.1	187.923
43	0.631	6.77	42.16	50.2	143.131
44	0.316	7.52	20.69	18.6	285.255
44	0.316	7.83	15.85	36.1	305.965
45	0.398	8.72	23.21	109.1	14.536
66	0.316	32.5	5.99	60	329.55
66	0.316	32.82	6.01	50.3	322.824
84	0.158	32.13	11.08	100.7	189.658
91	0.158	32.6	3.7	138.9	46.412
92	0.251	32.9	9.38	36.9	309.396
93	0.126	44.63	9.08	43	138.791
94	0.126	45.01	12.09	148.3	57.057
97	0.1	8.26	25.38	109.1	197.131
101	0.126	45.26	17.56	164.8	75.769
102	0.079	45.41	28.7	144.1	234.006
102	0.079	45.49	27.98	166.5	260.273
103	0.1	45.55	12.8	154.8	66.647
103	0.1	45.65	12.94	138.1	44.254
110	0.126	45.14	11.92	155.2	244.917
119	0.04	44.77	17.66	110.2	14.003

Section III

Tilt number	window size	depth	tilt angle	tilt axis	tilt way
1	19.953	18.210	11.110	32.100	128.094
5	12.589	47.070	6.930	153.700	243.700

8	2.512	29.450	8.030	148.000	56.786
8	2.512	31.960	15.100	137.800	44.601
11	6.310	12.420	21.470	179.700	271.562
12	6.310	18.730	26.580	12.900	112.355
13	3.981	26.200	15.630	153.200	243.687
19	2.512	21.910	5.600	148.100	58.592
24	2.512	39.490	4.780	163.400	74.464
26	0.794	12.700	37.100	13.900	286.488
31	1.259	1.120	8.800	116.800	201.948
36	0.794	20.640	29.050	117.900	22.161
41	0.631	13.680	7.450	25.300	136.359
41	0.631	14.310	39.920	4.900	100.750
44	0.398	23.410	17.920	158.500	71.068
49	0.794	21.440	22.870	150.500	240.078
52	0.398	43.720	4.440	49.800	141.210
53	0.794	0.790	8.830	67.700	159.993
62	0.200	55.430	4.210	145.200	53.391
62	0.200	55.620	6.670	139.000	46.686
63	0.398	1.120	7.510	136.500	222.675
63	0.398	1.520	9.030	158.700	249.742
67	0.631	22.510	32.600	159.400	249.817
71	0.200	11.930	25.590	17.300	112.273
72	0.126	12.330	55.970	176.600	266.589
80	0.316	41.630	7.160	164.500	255.199
84	0.251	0.180	12.590	26.800	123.194
88	0.316	11.590	10.120	17.300	291.064
90	0.251	14.500	49.610	5.800	101.530
94	0.316	39.420	10.160	14.500	109.428
95	0.398	39.740	10.430	77.200	344.813
97	0.158	42.140	4.230	136.200	225.227
97	0.158	42.300	4.020	157.800	248.264
122	0.316	56.180	18.260	162.200	253.868
134	0.079	55.280	10.890	48.600	143.342
137	0.100	0.590	8.260	13.800	108.958
141	0.158	12.020	16.930	178.700	90.980
141	0.158	12.180	26.380	163.600	74.013
146	0.158	42.930	2.040	163.700	74.595
146	0.158	43.090	3.470	179.200	90.947
160	0.063	56.080	28.700	144.100	234.006
160	0.063	56.140	27.980	166.500	260.273
171	0.040	56.000	34.310	176.100	87.709
172	0.040	56.280	27.840	121.100	20.920
183	0.050	55.680	19.500	143.000	50.403
184	0.100	55.790	13.940	154.700	244.339